nature nanotechnology

Article

https://doi.org/10.1038/s41565-022-01293-z

Emergence of layered nanoscale mesh networks through intrinsic molecular confinement self-assembly

Received: 24 June 2022

Accepted: 10 November 2022

Published online: 09 January 2023

Check for updates

Zehao Sun 1,5, Runze Liu 1,5, Tingyu Su 2, Hejin Huang, Ken Kawamoto, Ruigi Liang⁴, Bin Liu³, Mingjiang Zhong ⁶, Alfredo Alexander-Katz¹,

Block copolymer self-assembly is a powerful tool for two-dimensional nanofabrication; however, the extension of this self-assembly concept to complex three-dimensional network structures is limited. Here we report a simple method to experimentally generate three-dimensional layered mesh morphologies through intrinsic molecular confinement self-assembly. We designed triblock bottlebrush polymers with two Janus domains: one perpendicular and one parallel to the polymer backbone. The former enforces a lamellar superstructure that intrinsically confines the intralayer self-assembly of the latter, giving rise to a mesh-like monoclinic (54°) M¹⁵ network substructure with excellent long-range order, as well as a tetragonal (90°) T¹³¹ mesh. Numerical simulations show that the spatial constraints exerted on the polymer backbone drive the assembly of M¹⁵ and yield T¹³¹ in the strong segregation regime. This work demonstrates that intrinsic molecular confinement is a viable path to bottom-up assembly of new geometrical phases of soft matter, extending the capabilities of block copolymer nanofabrication.

Classical block copolymer self-assembly enables access to a range of well-known and useful ordered nanostructure geometries, such as spheres, cylinders (CYL), gyroids (GYR) and lamellae (LAM)¹⁻⁵. Nevertheless, there remains a large gap between the simple patterns commonly formed by block copolymers and the patterns required for many nanoscale applications. For example, single- and multilayer mesh nanostructures, which are defined as overlaid parallel lines with different orientations (Fig. 1f), are of particular interest in a range of technologies, such as photonic materials, superhydrophobic coatings, flexible electronics and cross-point devices⁶⁻¹⁰; their fabrication, however, has been a long-standing challenge. For single-layer nanomeshes, state-of-the-art techniques include successive shear or laser alignment of two CYL layers^{11,12} as well as directed self-assembly of CYL or LAM layers on topographically patterned substrates with post arrays or trenches^{7,8,13,14}; for multilayer nanomeshes, all the current techniques require repetitive layer-by-layer overlay steps^{7,15,16}. Thus far, a simple, straightforward fabrication process through 'bottom-up' macromolecular design rather than 'top-down' pre- or post-treatments has not been demonstrated.

Addressing this challenge is no easy task: conventional block copolymer phase diagrams offer few opportunities for the formation of ordered three-dimensional (3D) continuous network phases. Without constraints in any direction in space, unconfined microphase separation tends to give cubic-symmetric networks, among which GYR is the most frequently observed, although rarer diamond and primitive cubic have also been reported 17,18. The only exception among the reported

Department of Materials Science and Engineering, Massachusetts Institute of Technology, Cambridge, MA, USA. 2Department of Mechanical Engineering, Massachusetts Institute of Technology, Cambridge, MA, USA. 3Department of Chemistry, Massachusetts Institute of Technology, Cambridge, MA, USA. 4Department of Chemical and Environmental Engineering, Yale University, New Haven, CT, USA. 5These authors contributed equally: Zehao Sun, Runze Liu. Me-mail: caross@mit.edu; jaj2109@mit.edu

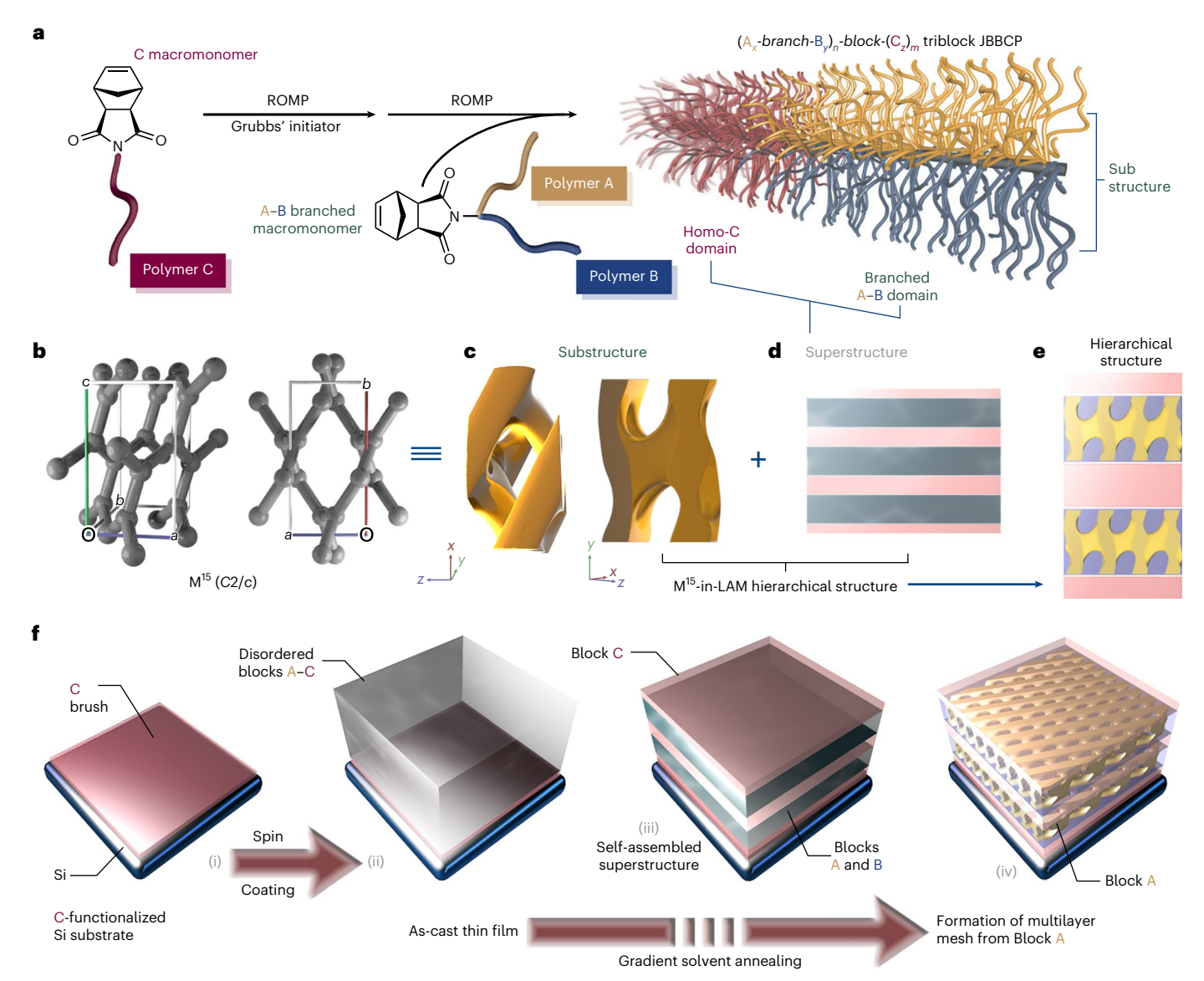


Fig. 1| Fabrication of multilayer nanomeshes based on intrinsic molecular confinement self-assembly of triblock JBBCPs. a, Schematic of the synthesis of triblock JBBCPs by sequential ring-opening metathesis polymerization (ROMP) of the C (red) macromonomer and then the branched A (yellow) – B (blue) macromonomer. b,c, Ball-and-stick model (b) and mathematical space-filling model (c) for an M^{15} network (monoclinic C2/c, space group 15) unit cell. d, Formation of the M^{15} substructure is driven by the intrinsic molecular confinement from the LAM superstructure. e, The M^{15} -in-LAM hierarchical

structure formed by the combination of superstructure and substructure from the self-assembled triblock JBBCP. **f**, Schematic of the fabrication procedures for multilayer nanomeshes. The flat silicon substrate is surface functionalized with a C-wetting layer (i) onto which a thin film of triblock JBBCP is spin coated (ii). The disordered mixture in (ii) is then annealed by a solvent vapour, first with a high vapour pressure to produce a LAM superstructure (iii) and then with a lowered vapour pressure to generate long-range ordered mesh-like M¹⁵ substructures in each superstructure layer (iv).

equilibrium network phases is O^{70} (orthorhombic Fddd, space group 70) as a single network of relatively low symmetry I^{19-21} (Supplementary Figs. 4a and 5a), but its phase region is narrow because its formation is associated with the instability of the GYR phase at the GYR/CYL boundary in the weak segregation limit I^{22} . Its derivative structure, I^{22} 0 (Pnna), was reported as a non-equilibrium phase stabilized by shear $I^{23,24}$.

Given that the mesh structures are anisotropic networks, their formation requires symmetry breaking. We gained inspiration from our previous studies on directed self-assembly, where nanoscale topographical constraints yield emergent symmetries^{8,25}, and considered whether analogous confinement could be intrinsically achieved via (macro)molecular design, noting that the study of low-symmetry network phases under confinement at the molecular level remains unexplored. Although non-network, comparatively simple nesting X-in-Y

(X, Y = LAM, CYL and so on) morphologies have long been predicted and observed for linear ABC terpolymers 26,27 , the inability to decouple the substructure (X) and superstructure (Y) formation greatly complicates the exploration of a large parameter space.

Here we introduce an 'intrinsic molecular confinement' self-assembly strategy that overcomes these challenges. Using our multiblock Janus bottlebrush copolymer (JBBCP)^{5,28,29} architectures, we achieve multilayer nanomesh structures where hierarchical X-in-Y self-assembly gives microphase-separated sub- and superstructures (Fig. 1a), each of which can be independently tuned. Using a suite of experimental characterization methods and dissipative particle dynamics (DPD) simulations, we show that roughly in the same phase region as the GYR structure produced by unconfined self-assembly, intrinsic molecular confinement provides access to a

mesh-like low-symmetry network with a 54° included angle that proved to be an M^{15} phase at equilibrium (monoclinic C2/c, space group 15: Fig. 1b,c), which has not been reported before in soft materials, to the best of our knowledge. Moreover, the intrinsic molecular confinement self-assembly approach (Fig. 1c-e) can produce large-scale, highly ordered single- or multilayer M15-in-LAM patterns with a sub-10-nm half-pitch on bare silicon substrates through a simple solvent annealing step, without the need for specialized substrates¹² or low-throughput templating techniques such as electron-beam lithography^{30,31}. Finally, a metastable network substructure, which is yet another mesh-like network but with a 90° included angle and tetragonal symmetry, was experimentally achieved; it was predicted to be thermodynamically stable only in the strong segregation regime by DPD simulations and identified as T¹³¹ (tetragonal P4₂/mmc, space group 131). These results pioneer intrinsic molecular confinement self-assembly as a new concept for the fabrication of complex soft materials.

Molecular design and synthesis of triblock JBBCPs

Triblock JBBCPs with the general formula $(A_x$ -branch- $B_y)_n$ -block- $(C_z)_m$ were synthesized and characterized, where A = polydimethylsiloxane (PDMS) with a number-average molar mass (M_n) of x = 5.0 kg mol⁻¹, B = polystyrene (PS) with varied $M_n(y)$ and C = poly(lactic acid) (PLA) with M_n of z = 6.3 kg mol⁻¹; here m and n are the number-average degrees of polymerization of the A-branch-B and C domains, respectively (Methods provides the synthesis details). These JBBCPs are designed such that a substructure forms through the microphase separation of A and B normal to the JBBCP backbone, which is intrinsically confined by a superstructure formed from the microphase separation of the A-branch-B domains from the C domain (Fig. 1a). Larger side-chain M_n values compared with previously reported triblock JBBCPs²⁹ were targeted to (1) facilitate access to the network phase region by finer control over the volume fractions; (2) obtain larger feature sizes (~101 nm, the resolution limit of electron microscopy for polymer materials), which can facilitate direct imaging characterization; and (3) drive stronger microphase separation, which provides a wider window for annealing and avoiding order-disorder transitions³². The substructure morphology was explored by varying the volume fraction of A in the A-branch-B domain (f_A) from 0.3 to 0.5, which was achieved using y = 4.6, 6.9, 8.2, 9.2 and 10.3 kg mol⁻¹. The effect of the superstructure, which confines the substructure, was examined by varying m and n. A complete list of the synthesized triblock JBBCPs is provided in Supplementary Table 1. For simplicity, we refer to these samples as $\mathbf{T} \mathbf{y}_{m \cdot n}$ where **T** represents triblock, the following digits indicate the M_n value of B (in units of kilogram per mole) and the subscript indicates the backbone degrees of polymerization. For example, **T6.9**₅₀₋₂₀ has the following composition: (PDMS_{5.0 kg mol}-i-branch-PS_{6.9 kg mol}-i)₂₀-block-

Single- and multilayer nanomesh pattern formation

With these samples in hand, intrinsic molecular confinement self-assembly was investigated following the fabrication steps outlined in Fig. 1f, with results from ${\bf T6.9_{30\cdot30}}$ described here as an example. First, a thin film of ${\bf T6.9_{30\cdot30}}$ was spin coated onto a silicon substrate grafted with a C-homopolymer brush, the latter of which is required to orient the JBBCP superstructure parallel to the substrate by removing surface diffusion barriers and lowering the surface energy of the C domain this surface functionalization, the orientation of the superstructure was poorly controlled (Supplementary Fig. 17b). Next, gradient solvent annealing in chloroform vapour was performed (Fig. 1c-e), where the swelling ratio of the film was controlled by nitrogen flow in a reservoir system (Methods) The films were first subjected to a high degree of swelling for 30 min to anneal and orient the confining superstructure, which was observed by scanning electron

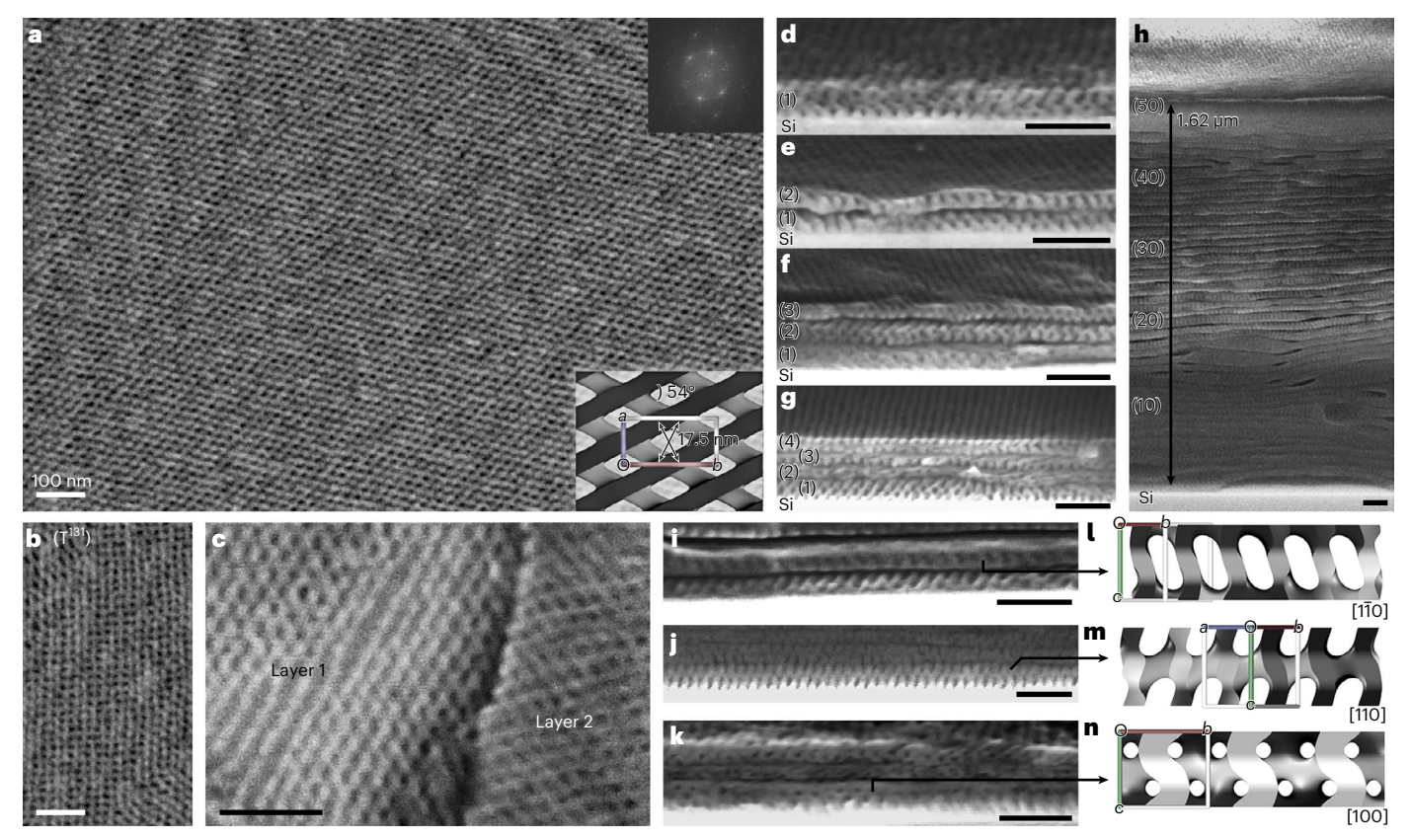
microscopy (SEM) to be horizontal LAM, as expected (Supplementary Fig. 17e). In the course of this process, we noticed an unusual mesh network substructure, but it did not display long-range order due to the weak segregation of the A and B domains under these conditions³⁶ (Supplementary Fig. 17c). Thus, to further drive the assembly of this substructure, we exposed the sample to subsequent reduced swelling annealing conditions for various times. Strikingly, this process produced reasonably ordered mesh substructures within 5 min (Supplementary Fig. 20), which improved further as the annealing time increased (Supplementary Fig. 17d). Ultimately, micrometre-scale ordered mesh network grains were obtained after 2 h (Fig. 2a and Supplementary Fig. 21). In contrast, such high-quality patterns could not be achieved by non-gradient annealing, that is, using the same swelling conditions throughout (Supplementary Fig. 19). Reactive ion etching (RIE; Methods) was used to remove the B and C (PS and PLA, respectively) domains and retain the mesh-forming A block by oxidizing the PDMS (ref. 33). Fast Fourier transform of the top-view SEM images of the films prepared from T6.9₃₀₋₃₀ (Fig. 2a, inset) revealed a mesh network pattern with an included angle of 54° and a line spacing of 17.5 nm. This simple and spontaneous formation of well-ordered meshes separated by superstructure layers contrasts with the sequential multistep overlay methods used previously to form nanoscale mesh structures^{7,13,15,16}.

Given that the super- and substructure formation are independently controlled in this system, the number of mesh-patterned layers, that is, the number of horizontal lamellae of the superstructure, can be arbitrarily tuned by simply adjusting the spin-coated film thickness. Examples of the formation of single- to four-layer nanomesh patterns, as evidenced by cross-sectional views, are shown in Fig. 2d–g. The number of layers can keep increasing as needed (Supplementary Figs. 32 and 33), although micrometre-scale-thick films require a longer annealing time (around 4 h in total). Remarkably, even a multilayer mesh pattern with as many as 50 layers could be easily fabricated using this method (Fig. 2h and Supplementary Fig. 31), a daunting task by any other nanofabrication technique.

For multilayer nanomeshes, angled etching was employed to create terraces on the thin-film surface 37 , confirming that the mesh was present in the lower layers (Fig. 2c). High-power CF_4/O_2 RIE reveals the internal morphology 38 (Supplementary Fig. 34). Cross-sectional SEM images (Fig. 2i–k) show patterns characteristic of the M^{15} network structure (Fig. 2l–n) throughout the film.

Identification of the M15 network structure

We identified the mesh-like substructure as an undiscovered low-symmetry monoclinic M¹⁵ network phase (M, monoclinic; space group 15 or C2/c), despite its cuboidal unit cell (Fig. 1b,c; Supplementary Data 1 provides the 3D models). Although M15 shares some similarities with the reported orthorhombic O⁷⁰ Fddd phase ¹⁹⁻²² in terms of its network connectivity and appearance of certain projections (Supplementary Figs. 4 and 5; Supplementary Information provides more details), M15 and O70 show disparate symmetries and phase behaviours, as described below. One way of visualizing the complex network structure is to view it as ABA-stacked layers of parallel lines that are twisted at an angle (Supplementary Fig. 6a). This organization is evident from the top surface of the cross-sectional SEM images, which display unidirectional parallel line patterns (Fig. 2d-h). Notably, these lines are not straight, but rather wavy in the out-of-plane direction (that is, the caxis of the lattice), forming hexagonally packed round holes as observed from the side (Fig. 2k,n). The 'twist angle', or the included angle θ of the nanomesh, is dictated by the ratio of the lattice parameters a and b, with θ = 2arctan(a/b). Free-energy arguments analogous to those made for O⁷⁰ phase stability²² as well as our DPD simulations (Supplementary Fig. 43) suggest a preferential ratio of a:b=1:2, in good accordance with the 54° angle observed in experiments (Fig. 2a). The mesh-like (001) plane of the M¹⁵ substructure was found to be exclusively parallel to the LAM superstructure (Supplementary Fig. 17b,d), probably due to the



 $\label{eq:Fig.2} \textbf{SEM imaging of the multilayer nanomesh structures. a}, \textit{Top view of a micrometre-scale long-range ordered 54° mesh network with an interline spacing of 17.5 nm (the top-right inset shows the fast Fourier transform). Its full-scale image is shown in Supplementary Fig. 21. The other inset is the top projection of a mathematical model for the <math display="inline">M^{\rm I5}$ network shown at higher magnification. **b**, Top view of a coexistent 90° mesh network with the same interline spacing, taking up 2% of the total area (full-scale image is shown in Supplementary Fig. 21). **c**, Top view of the terraced region after angled etch, showing the mesh networks in two

different layers, which exhibit no interlayer correlation. \mathbf{d} – \mathbf{h} , Cross-sectional views of single-, two-, three-, four-, and 50-layer nanomeshes, fabricated from thin films of different thicknesses. \mathbf{i} – \mathbf{n} , Cross-sectional views of the nanomeshes $(\mathbf{i}$ – \mathbf{k}), showing features in agreement with $[1\bar{1}0]$ (\mathbf{l}), [110] (\mathbf{m}) and [100] (\mathbf{n}) projections of the \mathbf{M}^{15} model, respectively. All the pictures were from the self-assembly of $\mathbf{T6.9}_{30\cdot30}$ thin films after RIE, showing bright A blocks (that is, oxidized PDMS). Scale bars, 100 nm.

polymer backbone configuration at the interface with the C domain (discussed in the next section), but the in-plane orientation of the M^{15} substructure was random, resulting in grains with various appearances in the cross-section (Fig. 2i-k).

Unfortunately, the analysis of the network substructure through scattering or diffraction techniques is not possible, as the substructure is not 3D periodic but sandwiched and confined by the LAM superstructure without interlayer correlations (Fig. 2c and Supplementary Fig. 44). This 'slicing effect' is clearly observed in the fast Fourier transform of a simulated M¹⁵-in-LAM structure, showing severe peak broadening and loss of information compared with that of a bulk M¹⁵ structure (Supplementary Fig. 25). Indeed, peak broadening was observed in the experimental small-angle X-ray scattering profile of the solvent-annealed **T6.9**₃₀₋₃₀ sample (Supplementary Fig. 48). Therefore, direct imaging techniques were necessary to characterize the network substructure.

The top (Fig. 2a) and cross-sectional (Fig. 2i–k) views of the SEM images show qualitative agreement with the [001], [1Ī0], [110] and [100] projections of the M¹⁵ model (Fig. 2a (inset) and Fig. 2l–n). A tilted view is shown in Supplementary Fig. 26. Although RIE slightly reduces the out-of-plane dimensions, we have previously found that etched samples provide a high-fidelity rendition of the original microdomain features³9. Nevertheless, as a comparison, unetched thin-film samples were sectioned by a focused ion beam and imaged by high-angle annular dark-field scanning transmission electron microscopy, showing clearer but similar cross-sectional patterns (Fig. 3a and Supplementary

Figs. 28 and 29) versus SEM. Scanning transmission electron microscopy (STEM) imaging of unetched single-layer nanomeshes fabricated on a silicon nitride membrane substrate exhibited a top view that was similar to the SEM images (Fig. 3h), although the interpretation of the STEM projections is less straightforward (Supplementary Figs. 29 and 30). The 3D tomography measurements of the sample (Fig. 3a) elucidate the structural features (Supplementary Video 1). The reciprocal space pattern of the substructure clearly confirms its monoclinic symmetry (Supplementary Fig. 24g–i), and the reconstructed real-space 3D geometry (Fig. 3b–d and Supplementary Video 2) closely resembles the mathematical model of the M¹5 substructure (Fig. 3e–g and Supplementary Video 2).

A possible mechanism for M15 phase formation

We hypothesized that the M¹⁵ substructure and its preferential interfacial (001) orientation formed in the A-branch-B domain are uniquely made possible through intrinsic molecular confinement imposed by the C domain and the resulting superstructure. To test this hypothesis, we synthesized an A-branch-B diblock JBBCP (ref. 5) (PDMS $_{5.0~\rm kg\,mol}^{-1}$ -branch-PS $_{6.9~\rm kg\,mol}^{-1}$) $_{30}$ (D6.9 $_{30}$) with the same chemical composition as the A-branch-B domain of T6.9 $_{30-30}$ and solvent annealed this polymer under the same conditions as T6.9 $_{30-30}$. Interestingly, this diblock JBBCP forms a cubic-symmetric GYR morphology instead of M¹⁵ (Fig. 4a,b), strongly supporting our hypothesis.

This difference—M¹⁵ morphology for an intrinsically confined triblock JBBCP versus GYR for an unconfined diblock variant—was

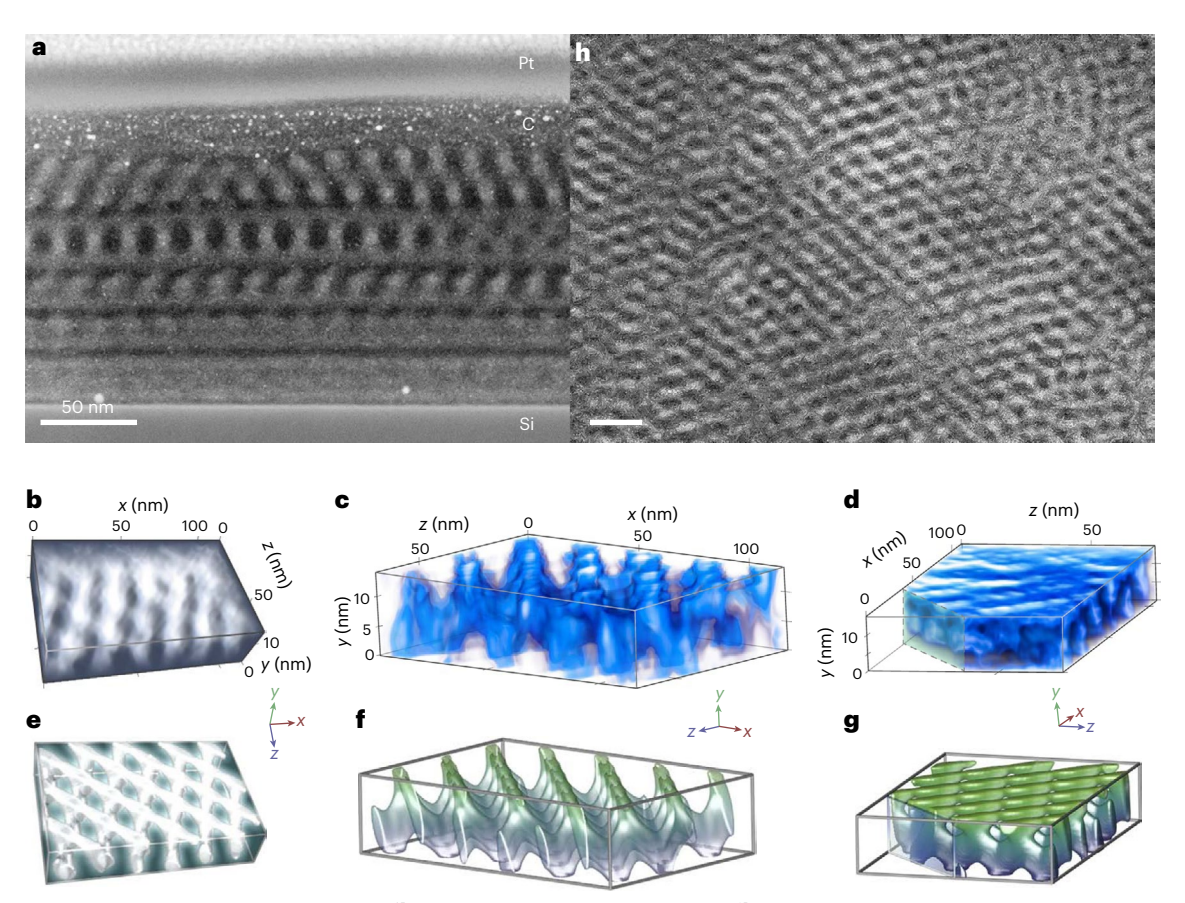


Fig. 3 | STEM imaging and tomography evidence for the M^{15} substructure. a, STEM imaging of an unetched, focused-ion-beam-cross-sectioned $T6.9_{30\cdot30}$ thin-film sample. b-d, Volume rendering of the 3D tomography reconstruction for the substructure network from the same sample as in a.e-g, Mathematical

model for the M¹⁵ network viewed from the same angles as \mathbf{b} – \mathbf{d} (\mathbf{e} – \mathbf{g}), respectively. \mathbf{h} , STEM plain view of the unetched single-layer nanomeshes fabricated from $\mathbf{T6.9}_{30\text{-}30}$ on a silicon nitride membrane substrate. Scale bars, 50 nm.

explored further using a reparametrized DPD model 40 (Methods). With a sensible choice of the modelling parameters, we were able to reproduce the GYR (Fig. 4c–e) and $\rm M^{15}$ -in-LAM morphologies (Fig. 4g–j and Supplementary Figs. 43 and 44) of diblock and triblock JBBCPs respectively, supporting our experimental interpretation. The DPD model was also successful in explaining the non-uniform thicknesses of the LAM superstructure for the triblock (Fig. 3a) with incommensurate height restrictions, that is, when the total thickness is not exactly an integer multiple of the equilibrium LAM spacing (Supplementary Fig. 51).

As a particle-based approach, the DPD model offers insights into the geometry of individual polymer chains. Interestingly, the backbones of the simulated GYR-forming diblock JBBCP were found to be rather more coiled at the three-way nodes (Fig. 4e) than in the interconnecting struts (Fig. 4d), similar to a previous conclusion from the simulation of linear diblock copolymers known as packing frustration⁴¹. For the corresponding triblock JBBCP with the same A-to-B volume ratio (that is, f_A (diblock) = f_A '(triblock)), the presence of the LAM superstructure requires that the ends of the backbones in the A-branch-B domain must be pinned at the interface, making it difficult for these backbones to bend to accommodate the node structure. This intrinsic molecular confinement results in a more extended configuration of the backbones for the triblock JBBCPs (Fig. 4h-j and Supplementary Fig. 50) and globally stabilizes the M¹⁵ phase over GYR. These results reflect a strong effect of the molecular-level backbone geometry on the final mesoscale morphology: coiled backbones produce a more curved GYR morphology, whereas rigid, extended backbones create sharper junctions and give rise to an M15 phase with straighter network struts.

Phase diagrams of di- and triblock systems

To identify the phase region for the M^{1S} structure, the intrinsic molecular confinement self-assembly of triblock JBBCPs with different f_A' values and backbone degrees of polymerization (that is, m and n) were compared with the corresponding unconfined diblock JBBCPs $\mathbf{D}\mathbf{y}_n$ (a diblock with B-branch M_n of y kg mol $^{-1}$ and a backbone degree of polymerization n). A complete list of the tested samples is shown in Supplementary Table 1. For all m and n tested, the observed superstructures for triblock JBBCPs were LAM due to the rigidity of the poly(norbornene) backbone 4 ; the backbone degree of polymerization had little impact on the final morphologies (Supplementary Figs. 37–39), in accordance with previous observations 5,29 .

Next, the morphology as a function of the volume fraction f_A (diblock) or f_A ′(triblock) was studied (Supplementary Figs. 36–40); the results are summarized in Fig. 4f. The effective volume fraction in a swelled film varies with the solvent annealing condition; therefore, a quantitative model⁴² was applied to account for this effect (Supplementary Fig. 8, Supplementary Table 2 and Supplementary Information). Constructed from these effective volume fractions, the experimental and simulated (Supplementary Figs. 41 and 42) phase diagrams quantitatively match well with each other (Fig. 4f), that is, they share roughly the same phase regions for each phase, indicating that the phase behaviour can be generalized for different chemical blocks. More importantly, both show a one-to-one mapping between the diblock and triblock phase regions. For the triblock JBBCP discussed in this paper, the M¹⁵ substructure phase emerges at an effective f_A value of 32% and ends at ~39%, conforming well with the GYR phase region of the diblock JBBCP. The polymers with f_A ' < 32% or f_A ' > 39% showed CYL-in-LAM or

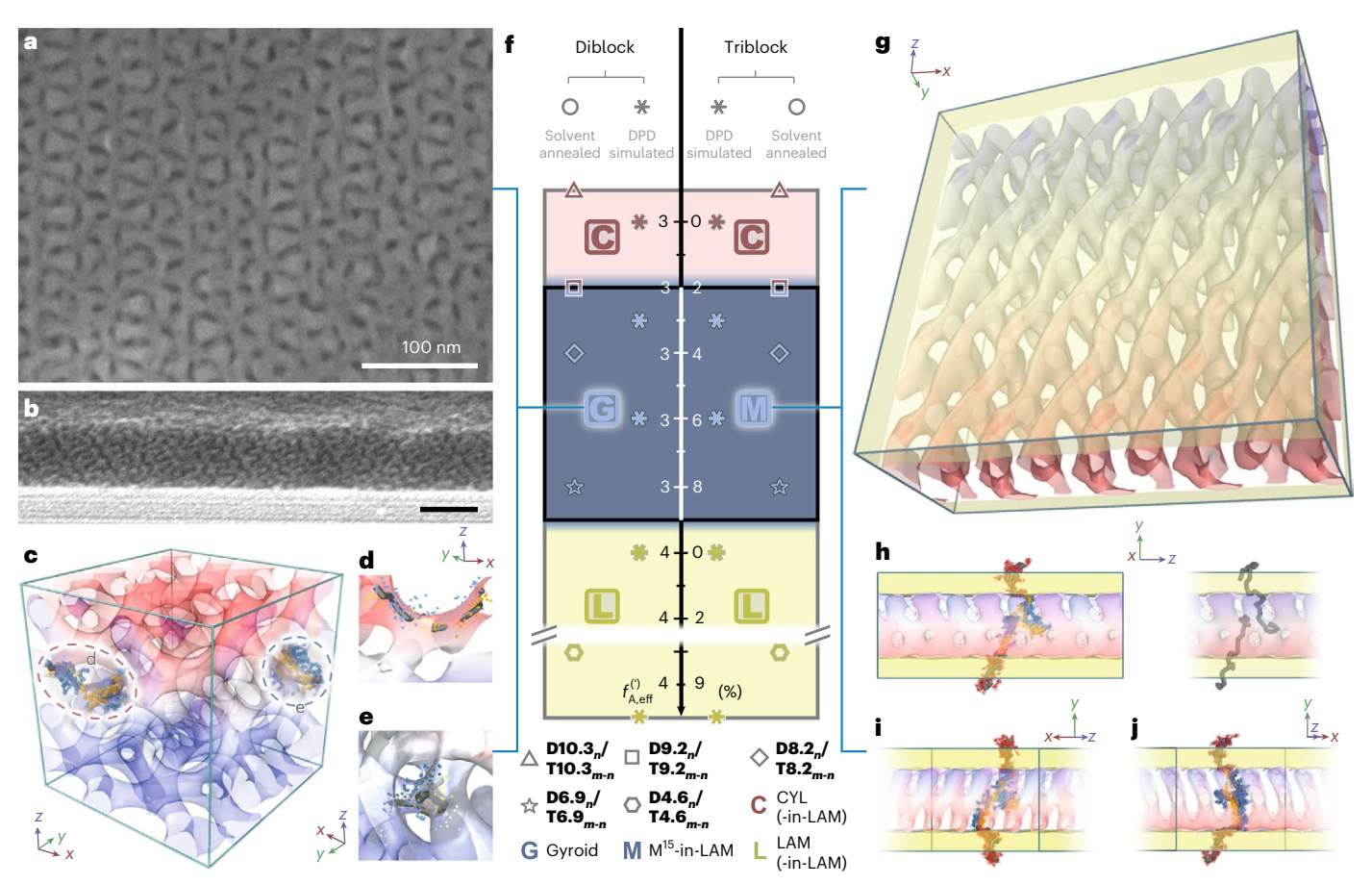


Fig. 4 | **Comparison of the networks and phase diagrams between di- and triblock JBBCPs. a, b,** Top and cross-sectional SEM images of the GYR-forming $\mathbf{D6.9_{30}}$ thin film. Scale bars, 100 nm. **c**, DPD-simulated GYR structure for a diblock JBBCP with $f_{\Lambda} = 33\%$. **d,e**, Two typical configurations of macromolecules, where the backbones are shown in grey, and the A and B branches are shown as yellow and blue dots, respectively. The strut-forming backbones are extended (**d**) and the node-forming backbones are coiled (**e**). **f**, Experimental and simulated phase diagrams for di- and triblock JBBCPs, showing a one-to-one mapping

relationship. In particular, the phase region of the M^{15} network substructure matches well with that of GYR. The morphology of each data point is shown in Supplementary Figs. 36–42. \mathbf{g} , DPD-simulated M^{15} -in-LAM structure for a triblock JBBCP with $f_A' = 33\%$. \mathbf{h} - \mathbf{j} , Typical configurations of macromolecules corresponding to the [100] (\mathbf{h}), [110] (\mathbf{i}) and [1 $\bar{\mathbf{l}}$ 0] (\mathbf{j}) projections of the M^{15} network, where the backbones are extended and shown in grey, and the A, B and C branches are shown in yellow, blue and red, respectively. In all the DPD-simulated structures (\mathbf{c} - \mathbf{e} and \mathbf{g} - \mathbf{j}), the space filled by the B block is removed for clarity.

LAM-in-LAM hierarchical morphologies (Supplementary Figs. 40 and 36, respectively), as reported elsewhere 29 . It is noteworthy that the M^{15} phase region is wide and overlapping with the GYR phase region, which is fundamentally different from previously reported network phases, such as O^{70} , which have narrow windows of stability and border the GYR phase. This finding suggests that intrinsic molecular confinement self-assembly can literally replace a known phase of the classical block copolymer phase diagram with a new phase.

The above studies utilized solvent annealing, and we found that thermal annealing yielded qualitatively similar trends (Supplementary Figs. 45–47), although with poorer order and sometimes mixed morphologies, demonstrating that those phases are indeed thermodynamically stable. An interesting phenomenon observed for both solvent and thermally annealed M¹⁵-in-LAM-forming samples was the coexistence of the 54° mesh network (from the M¹⁵ substructure) alongside a small fraction of a 90° mesh network (Fig. 2b and Supplementary Figs. 22, 55 and 56). A detailed structural analysis was not possible given its rare occurrence; however, we managed to capture a similar intermediate state in the DPD model during its evolution (Supplementary Fig. 52), indicating that it represents a metastable phase. This new tetragonal T¹³¹ (P4₂/mmc, space group 131) structure has a distinct network connectivity compared with M¹⁵ (Supplementary Figs. 4, 6 and 53 and Supplementary Information) and can be described by a Schwarz 'crossed

layers of parallels' minimal surface. Furthermore, our DPD model predicts a more energetically favourable T^{131} substructure than M^{15} if the Flory–Huggins mixing parameter χN is greater than a critical value (Supplementary Fig. 54), suggesting that T^{131} might be experimentally promoted under higher segregation conditions. Indeed, we observed a larger fraction of T^{131} after thermal annealing (Supplementary Fig. 56), where the effective χ value is larger without the interaction-screening solvent molecules⁴².

The calculation of free energies under different Flory–Huggins mixing parameters in DPD simulations provides another rationalization of the emergence of these network phases in triblock JBBCPs. Although an M¹⁵ or T¹³¹ network could be obtained in simulations using the diblock architecture (Supplementary Fig. 53), due to the existence of a low-energy GYR phase, they could not be stabilized unless an unusually high χN is set; consequently, they are completely missing in experiments. In contrast, the intrinsic molecular-confinement-induced destabilization of GYR in the triblock JBBCPs allows the formation of these high-energy phases.

Conclusion

We have presented the self-assembly of a triblock bottlebrush copolymer system, achieving the formation of a highly ordered multilayer (1-to 50-layer) mesh pattern on a flat silicon substrate in a simple annealing

process. The mesh substructure is a novel monoclinic M¹⁵ network phase and forms over a relatively wide compositional window, which roughly matches the GYR phase region for its diblock counterpart. Simulations reveal that the stabilization of this low-symmetry network phase is due to the restrictions imposed on the geometry of the backbone at the interfaces with the lamellar superstructure. This work offers not only a simple solution for the fabrication of challenging 3D structures that could facilitate manufacturing of nanoscale devices but also a path to the discovery of other new network phases in soft-matter systems.

Online content

Any methods, additional references, Nature Portfolio reporting summaries, source data, extended data, supplementary information, acknowledgements, peer review information; details of author contributions and competing interests; and statements of data and code availability are available at https://doi.org/10.1038/s41565-022-01293-z.

References

- Bates, F. S. & Fredrickson, G. H. Block copolymers—designer soft materials. *Phys. Today* 52, 32–38 (1999).
- 2. Hamley, I. W. Nanostructure fabrication using block copolymers. *Nanotechnology* **14**, R39–R54 (2003).
- 3. Segalman, R. A. Patterning with block copolymer thin films. *Mater. Sci. Eng. R Rep.* **48**, 191–226 (2005).
- Bolton, J., Bailey, T. S. & Rzayev, J. Large pore size nanoporous materials from the self-assembly of asymmetric bottlebrush block copolymers. Nano Lett. 11, 998–1001 (2011).
- Kawamoto, K. et al. Graft-through synthesis and assembly of Janus bottlebrush polymers from A-branch-B diblock macromonomers. J. Am. Chem. Soc. 138, 11501–11504 (2016).
- Cheng, L.-C. et al. Imparting superhydrophobicity with a hierarchical block copolymer coating. Small 16, 1905509 (2020).
- Tavakkoli, K. G. et al. Multilayer block copolymer meshes by orthogonal self-assembly. Nat. Commun. 7, 10518 (2016).
- Tavakkoli, K. G. et al. Templating three-dimensional self-assembled structures in bilayer block copolymer films. Science 336, 1294–1298 (2012).
- Zhang, L. et al. A nanomesh scaffold for supramolecular nanowire optoelectronic devices. Nat. Nanotechnol. 11, 900–906 (2016).
- Bai, X. et al. Room-temperature processing of silver submicron fiber mesh for flexible electronics. npi Flex. Electron. 2. 3 (2018).
- 11. Kim, S. Y. et al. Large-area nanosquare arrays from shear-aligned block copolymer thin films. *Nano Lett.* **14**, 5698–5705 (2014).
- Majewski, P. W., Rahman, A., Black, C. T. & Yager, K. G. Arbitrary lattice symmetries via block copolymer nanomeshes. *Nat. Commun.* 6, 7448 (2015).
- Liu, R., Huang, H., Sun, Z., Alexander-Katz, A. & Ross, C. A. Metallic nanomeshes fabricated by multimechanism directed self-assembly. ACS Nano 15, 16266–16276 (2021).
- Cha, S. K. et al. Nanopatterns with a square symmetry from an orthogonal lamellar assembly of block copolymers. ACS Appl. Mater. Interfaces 11, 20265–20271 (2019).
- Subramanian, A., Tiwale, N., Doerk, G., Kisslinger, K. & Nam, C.-Y. Enhanced hybridization and nanopatterning via heated liquid-phase infiltration into self-assembled block copolymer thin films. ACS Appl. Mater. Interfaces 12, 1444–1453 (2020).
- Jeong, J. W. et al. High-resolution nanotransfer printing applicable to diverse surfaces via interface-targeted adhesion switching. Nat. Commun. 5, 5387 (2014).
- Chu, C. Y. et al. Real-space evidence of the equilibrium ordered bicontinuous double diamond structure of a diblock copolymer. Soft Matter 11, 1871–1876 (2015).
- Chang, C.-Y. et al. Mesoscale networks and corresponding transitions from self-assembly of block copolymers. Proc. Natl Acad. Sci. USA 118, e2022275118 (2021).

- Bailey, T. S., Hardy, C. M., Epps, T. H. & Bates, F. S. A noncubic triply periodic network morphology in pol y(isoprene-b-styrene-b-ethylene oxide) triblock copolymers. *Macromolecules* 35, 7007–7017 (2002).
- Takenaka, M. et al. Orthorhombic Fddd network in diblock copolymer melts. Macromolecules 40, 4399–4402 (2007).
- 21. Epps, T. H. et al. Ordered network phases in linear pol y(isoprene-b-styrene-b-ethylene oxide) triblock copolymers. *Macromolecules* **37**, 8325–8341 (2004).
- 22. Tyler, C. A. & Morse, D. C. Orthorhombic Fddd network in triblock and diblock copolymer melts. Phys. Rev. Lett. **94**, 208302 (2005).
- Meuler, A. J., Hillmyer, M. A. & Bates, F. S. Ordered network mesostructures in block polymer materials. *Macromolecules* 42, 7221–7250 (2009).
- Bluemle, M. J., Fleury, G., Lodge, T. P. & Bates, F. S. The O⁵² network by molecular design: CECD tetrablock terpolymers. Soft Matter 5, 1587–1590 (2009).
- 25. Ding, Y. et al. Emergent symmetries in block copolymer epitaxy. *Nat. Commun.* **10**, 2974 (2019).
- Zheng, W. & Wang, Z.-G. Morphology of ABC triblock copolymers. Macromolecules 28, 7215–7223 (1995).
- Mogi, Y. et al. Superlattice structures in morphologies of the ABC triblock copolymers. Macromolecules 27, 6755–6760 (1994).
- Guo, Z.-H. et al. Janus graft block copolymers: design of a polymer architecture for independently tuned nanostructures and polymer properties. *Angew. Chem. Int. Ed.* 57, 8493–8497 (2018).
- 29. Liang, R. et al. Hierarchically engineered nanostructures from compositionally anisotropic molecular building blocks. *Nat. Mater.* **21**, 1434–1440 (2022).
- 30. Chen, Y. Nanofabrication by electron beam lithography and its applications: a review. *Microelectron. Eng.* **135**, 57–72 (2015).
- Li, K. et al. High speed e-beam writing for large area photonic nanostructures—a choice of parameters. Sci. Rep. 6, 32945 (2016).
- Sinturel, C., Bates, F. S. & Hillmyer, M. A. High χ-low N block polymers: how far can we go? ACS Macro Lett. 4, 1044–1050 (2015).
- 33. Jung, Y. S. & Ross, C. A. Orientation-controlled self-assembled nanolithography using a polystyrene–polydimethylsiloxane block copolymer. *Nano Lett.* **7**, 2046–2050 (2007).
- Gu, W., Hong, S. W. & Russell, T. P. Orienting block copolymer microdomains with block copolymer brushes. ACS Nano 6, 10250–10257 (2012).
- 35. Gotrik, K. W. et al. Morphology control in block copolymer films using mixed solvent vapors. *ACS Nano* **6**, 8052–8059 (2012).
- Gu, X., Gunkel, I., Hexemer, A., Gu, W. & Russell, T. P. An in situ grazing incidence X-ray scattering study of block copolymer thin films during solvent vapor annealing. *Adv. Mater.* 26, 273–281 (2014).
- 37. Lee, S. et al. Resolving triblock terpolymer morphologies by vapor-phase infiltration. *Chem. Mater.* **32**, 5309–5316 (2020).
- Son, J. G., Gotrik, K. W. & Ross, C. A. High-aspect-ratio perpendicular orientation of PS-b-PDMS thin films under solvent annealing. ACS Macro Lett. 1, 1279–1284 (2012).
- 39. Gotrik, K. W. et al. 3D TEM tomography of templated bilayer films of block copolymers. *Adv. Funct. Mater.* **24**, 7689–7697 (2014).
- Huang, H. & Alexander-Katz, A. Dissipative particle dynamics for directed self-assembly of block copolymers. J. Chem. Phys. 151, 154905 (2019).
- Martínez-Veracoechea, F. J. & Escobedo, F. A. Simulation of the gyroid phase in off-lattice models of pure diblock copolymer melts. J. Chem. Phys. 125, 104907 (2006).

42. Hannon, A. F., Bai, W., Alexander-Katz, A. & Ross, C. A. Simulation methods for solvent vapor annealing of block copolymer thin films. *Soft Matter* 11, 3794–3805 (2015).

Publisher's note Springer Nature remains neutral with regard to jurisdictional claims in published maps and institutional affiliations.

Springer Nature or its licensor (e.g. a society or other partner) holds exclusive rights to this article under a publishing agreement with the author(s) or other rightsholder(s); author self-archiving of the accepted manuscript version of this article is solely governed by the terms of such publishing agreement and applicable law.

© The Author(s), under exclusive licence to Springer Nature Limited 2022

Methods

Synthesis

The PLA macromonomer⁴³ \mathbf{M}_{PLA} ($M_n = 6.3 \text{ kg mol}^{-1}$) and the PDMS-PS branched macromonomers⁵ \mathbf{M}_y (M_n (PDMS) = 5.0 kg mol⁻¹, M_n (PS) = y kg mol⁻¹) used here were synthesized as reported in our previous works. The Grubbs' third-generation bispyridyl initiator (G3), (IMesH₂)(py)₂Cl₂Ru = CHPh, was synthesized according to procedures in the literature⁴⁴. All the reagents were purchased from commercial suppliers and used without further purification.

Diblock IBBCPs were synthesized by graft-through ring-opening metathesis polymerization (ROMP) using a slightly modified protocol⁵ (Supplementary Information). The synthesis of triblock JBBCPs with backbone degrees of polymerization of m and n, (PDMS_{5.0 kg mol}⁻¹ -branch-PS_y)_n-block-(PLA_{6.3 kg mol}⁻¹)_m, was carried out in 2 ml vials equipped with Teflon stir bars. $\mathbf{M}_{PLA}(0.030 \times m \, \mu \text{mol})$ was dissolved in anhydrous dichloromethane (DCM) in a glovebox under nitrogen atmosphere, followed by the addition of a stock solution of G3 in DCM (30 nmol) via a micropipette. The total volume of DCM added was ~40 μl. After 0.5 h, the reaction mixture was first diluted with 20 μl DCM, followed by the addition of the second macromonomer \mathbf{M}_{ν} $(0.030 \times n \,\mu\text{mol})$. The reaction was allowed to proceed for 5 min and then the reaction mixture was further diluted with 40 µl DCM. After further reaction for 4 h at room temperature, the mixture was removed from the glovebox and quenched with excess ethyl vinyl ether and then dried, characterized and subjected to self-assembly without further purification. A detailed description and discussion, as well as a list of the synthesized samples and their characterization, are available in the Supplementary Information.

Thin-film sample preparation

The JBBCPs were dissolved in chloroform and then spin coated on either silicon substrates or Si $_3$ N $_4$ TEM grids (with a 70-nm-thick nitride support film acting as the window) to form films with thicknesses ranging from 20 nm to 2 μ m. For triblock JBBCP samples, the substrates were surface modified by M_{PLA} , which was spun cast on the substrates, annealed at 130 °C for 24 h and rinsed with toluene to remove the unreacted material. In this process, the hydroxyl terminal group in M_{PLA} reacted with the silanol groups at the substrate surface via thermally induced dehydration 45 , leading to the formation of a PLA surface brush layer.

The thin films were solvent annealed in a closed glass chamber with a solvent reservoir of 2 ml chloroform. The solvent vapour pressure and consequently the extent of film swelling (S_R) were adjusted by nitrogen flow through the chamber with the rate (q_{N_2}) ranging from 3 to 10 s.c.c.m. controlled by a mass flow controller. The S_R value was monitored in situ by spectral reflectometry. The film was quenched by removing the lid of the chamber and taking the sample out of the chamber.

Typically, for triblock JBBCPs, the films were first annealed at $q_{\rm N_2}=3$ s.c.c.m. (high chloroform vapour pressure and high $S_{\rm R}$) for 30 min to anneal the superstructure and then at $q_{\rm N_2}=7$ s.c.c.m. (low chloroform vapour pressure and low $S_{\rm R}$) for another 30 min to anneal the substructure, unless otherwise stated. For diblock JBBCPs, which do not form superstructures, no notable difference was found with or without the first high- $S_{\rm R}$ annealing step. The effective volume fractions under this annealing condition are calculated based on the $S_{\rm R}$ value using a modified model⁴² (Supplementary Information).

RIE and SEM imaging

The silicon substrates with JBBCP films were cracked in liquid nitrogen. The cracked edge of one half and the top surface of the other half were reactive ion etched by an $8\,s$ CF $_4$ plasma (15 mtorr pressure, 15 s.c.c.m. gas flow and 50 W power) to remove the PDMS wetting surface layer and then a $30\,s$ O $_2$ plasma (6 mtorr pressure, 10 s.c.c.m. gas flow and 90 W power) to remove the PS and PLA and oxidize the PDMS microdomains, unless otherwise stated.

For multilayer mesh samples, in addition to the surface morphology, the internal morphology was investigated by angled etching 37 and high-power etching 38 . The terraced regions (Fig. 2c) were obtained by covering the half of the sample, etching the other half with high-power CF_4/O_2 plasma (8 s, 10 mtorr, 10 and 15 s.c.c.m. gas flow for CF_4 and O_2 , respectively, 450 W), removing the cover, further etching the entire sample according to the previous paragraph, and imaging the boundary between these two regions. The morphology in even lower layers could be observed by extending the time of high-power CF_4/O_2 etching or repeating this process.

The etched sample was then imaged using SEM at 3 or 5 kV. The cross-sectional view was imaged by tilting the sample by 75°.

STEM imaging and tomography

The STEM samples for top-view imaging were made by spin coating on a nitride substrate and solvent annealing, as described above. To avoid the overlapping of multiple mesh layers with different orientations, the film thickness was controlled such that a single-layer mesh was formed. The samples for cross-sectional imaging and tomography experiments were made by a focused ion beam from an unetched thin-film sample on a silicon substrate. The unetched sample was first sputter coated with a carbon protection layer of ~40 nm. The thin-section specimens were prepared using the lift-out method with a focused Au^+ beam operating at 35 kV and then welded on a copper grid.

STEM imaging and tomography were performed with an aberration-corrected Thermo Fisher Themis Z G3 60–300 kV instrument operated at 200 kV. The high-angle annular dark-field images were collected with a 50 pA beam current and a collection angle range of 30–185 mrad. The convergence angle was set to 16 mrad for static image acquisition or 12 mrad for tomography experiments for increased depth of focus. The STEM tomography program (Thermo Fisher) was used for tomography acquisition. The images were collected at each degree of tilt between -45° and 60° . We stopped at -45° because further increasing the tilting magnitude caused one end of the sample membrane to block the beam. The 3D reconstruction of tomography data was carried out by the algebraic reconstruction technique.

DPD simulation

The simulations were carried out using the LAMMPS package⁴⁶ with graphics processing unit acceleration⁴⁷. All the simulations represent a canonical (NVT) ensemble, and all the quantities are unitless in the model, with the fundamental quantities such as mass, distance and thermal energy $k_{\rm B}T$ set to unity. DPD is a coarse-grained particle-based simulation technique, which overcomes the time- and space-scale limitation encountered in molecular dynamics simulations and is powerful in tracking the morphology evolution⁴⁸. The triblock copolymer is modelled as a series of beads representing the side chains and backbone, connected by linear harmonic bonds. We fixed the number of backbone beads in the homo-C domain and the branched A-B domain to be m = n = 20 and the number of C-branch beads $N_c = 10$, and we varied the number of A- and B-branch beads $((N_A, N_B) = (3, 7), (4, 8), (4,$ 7), (4, 6) or (6, 6)) to quantitatively tune the volume fractions (f_A ' = 30%, 33%, 36%, 40% or 50%, respectively). The time evolution of the beads is governed by Newtonian motion due to conservative, dissipative and random forces, all of which are pairwise additive, short range and cut at $r_0 = 1.0$. In the reparametrized model⁴⁰ used here, the bead density was set to be ρ = 5, the repulsion parameter for the same bead type a_{ii} = 15 and the harmonic bond potential was set with the spring constant $K^{\rm B}$ = 50 and equilibrium distance r_0 = 1.0. To qualitatively mimic the immiscibility between different types of monomer in this system, we set DPD repulsive interaction parameters $a_{AB} = 22.5$ and $a_{AC} = a_{BC} = 26.0$, unless otherwise stated. The relationship between the repulsion parameters and Flory-Huggins parameter χ between two different beads is defined by equation $a_{ii} \approx a_{ii} + 1.45 \chi_{ii}$. No interaction was set between the backbone beads and side-chain beads; thus,

the backbone beads were not included in the calculation of volume fractions. To qualitatively mimic the stiffness of bonds in the backbone, a quadratic angle potential between two adjacent bonds was applied, namely, $V^A = K^A(\theta - \theta_0)^2$, where K^A is the potential constant, θ is the angle between two neighbouring bonds and equilibrium angle θ_0 was set to be π . Since the stiffness is dependent on the grafting density²⁹, we set $K^A = 1$ for the homo-C-domain backbone and $K^A = 2$ for the branched A–B-domain backbone.

The noise parameter σ was set to be 0.1 throughout the 12,000,000 simulation steps to find the stable morphology in the *NVT* system. The DPD time step was fixed at 0.01, and the LAMMPS default velocity Verlet integrator was used. Around 10% solvent beads that are neutral to all types of bead were added to the system to improve the mobility of JBBCPs and avoid the formation of potential trapped metastable states¹³. For the simulation of diblock JBBCPs, we set a cubic simulation box with dimensions of $L_x = L_y = L_z = 13$; for triblocks, tetragonal boxes were used with an in-plane size of $L_x = L_z = 13$, and the height $L_y = 24$ or 46 was set to be commensurate with one or two layers of LAM superstructure. Periodic boundary conditions were applied in all the three directions for all the simulations. More details of the DPD setup, for example, the rationale for the choice of simulation parameters, are described in the Supplementary Information.

Data availability

The raw data for STEM tomography and 3D reconstruction is provided in Supplementary Video 1. The LAMMPS input and output datasets are too large to be shared publicly but are available from the corresponding authors upon request. All other data needed to evaluate the conclusions of this study are available within the Article and its Supplementary Information.

Code availability

The code generated during this study is available via GitHub at https://github.com/Z-H-Sun/IMCmesh.

References

- Vohidov, F. et al. ABC triblock bottlebrush copolymerbased injectable hydrogels: design, synthesis, and application to expanding the therapeutic index of cancer immunochemotherapy. *Chem. Sci.* 11, 5974–5986 (2020).
- Sanford, M. S., Love, J. A. & Grubbs, R. H. A versatile precursor for the synthesis of new ruthenium olefin metathesis catalysts. Organometallics 20, 5314–5318 (2001).
- Edwards, E. W., Montague, M. F., Solak, H. H., Hawker, C. J. & Nealey, P. F. Precise control over molecular dimensions of block-copolymer domains using the interfacial energy of chemically nanopatterned substrates. *Adv. Mater.* 16, 1315–1319 (2004).

- Thompson, A. P. et al. LAMMPS—a flexible simulation tool for particle-based materials modeling at the atomic, meso, and continuum scales. Comp. Phys. Comm. 271, 108171 (2022).
- Brown, W. M., Wang, P., Plimpton, S. J. & Tharrington, A. N. Implementing molecular dynamics on hybrid high performance computers—short range forces. *Comput. Phys. Commun.* 182, 898–911 (2011).
- 48. Hoogerbrugge, P. J. & Koelman, J. M. V. A. Simulating microscopic hydrodynamic phenomena with dissipative particle dynamics. *Europhys. Lett.* **19**, 155–160 (1992).

Acknowledgements

J.A.J. acknowledges support from Eni S.p.A. through the MIT Energy Initiative. C.A.R. and A.A.-K. acknowledge support from NSF DMREF award 2118678. M.Z. acknowledges support from the NSF DMR award 2003875. This work was carried out in part through the use of MIT. nano's facilities and APS, a US Department of Energy (DOE) Office of Science User Facility operated for the DOE Office of Science by Argonne National Laboratory (contract no. DE-AC02-06CH11357). The shared facilities of CMSE, NSL and MRSEC under award DMR1419807 were used. We acknowledge the MIT Satori, the MIT SuperCloud, MIT Research Computing Project and Lincoln Laboratory Supercomputing Center for providing the high-performance computing resources that have contributed to the research results reported here. We thank E. Cho and A. Penn for help with STEM imaging and Y. Ouyang for helpful discussion.

Author contributions

Z.S., K.K. and B.L. synthesized the JBBCPs. Z.S., R. Liu and T.S. prepared the samples. Z.S., R. Liu, T.S. and R. Liang conducted the structure and property characterization. Z.S., R. Liu, H.H. and A.A.-K. conducted the simulations. Z.S., R. Liu, M.Z., C.A.R. and J.A.J. conceived the idea. Z.S., C.A.R. and J.A.J. wrote the manuscript.

Competing interests

The authors declare no competing interests.

Additional information

Supplementary information The online version contains supplementary material available at https://doi.org/10.1038/s41565-022-01293-z.

Correspondence and requests for materials should be addressed to Caroline A. Ross or Jeremiah A. Johnson.

Peer review information *Nature Nanotechnology* thanks Maria Sammalkorpi and the other, anonymous, reviewer(s) for their contribution to the peer review of this work.

Reprints and permissions information is available at www.nature.com/reprints.